Supplemental Information: Tunable magneto-optical properties in MoS_2 via defect-induced exciton transitions

Tomer Amit,[1] Daniel Hernangómez-Pérez,[1] Galit Cohen,[1] Diana Y. Qiu,[2] and Sivan Refaely-Abramson[1]

[1]*Department of Molecular Chemistry and Materials Science, Weizmann Institute of Science, Rehovot 7610001, Israel*

[2]*Department of Mechanical Engineering and Materials Science, Yale University, New Haven, Connecticut 06511, United States*

I. Computational details: quasiparticle and optical properties

Our calculations are employed within many-body perturbation theory, where density functional theory (DFT) serves as a starting point [1]. We first compute the electronic wavefunctions and Kohn-Sham energies from DFT with the Perdew-Burke-Ernzerhof (PBE) exchange-correlation functional [2] within the Quantum Espresso package [3, 4], including spin-orbit coupling and explicit spinor wavefunctions. The computed system contains a relaxed $5 \times 5 \times 1$ supercell of monolayer MoS_2 with one sulphur vacancy per supercell, and 15Å separation between periodic layers in the out-of-plane direction. The calculations were done with a Bloch plane-wave basis-set, using norm-conserving pseudopotentials from PseudoDojo [5] and with a 75 Ry energy cutoff. The self-consistent calculations of the electron density were done on a $6 \times 6 \times 1$ uniform k-grid. The quasiparticle bandstructure and optical properties were computed within the GW-BSE approximation using the BerkeleyGW software [6]. Quasiparticle energy corrections were calculated within G_0W_0 and the generalized plasmon-pole approximation [7], on a uniform $3\times3\times1$ k-point grid and with 3998 spinor bands and 25 Ry cutoff of the screening function. We then expand our sampling through the Nonuniform Neck Subsampling (NNS) scheme [8] to capture the behavior of the electron wavefunctions accurately throughout the Brillouin zone, as used previously for such supercell system [9]. Optical properties were computed by solving the Bethe-Salpeter equation (BSE) [10]. The electron-hole interaction kernel was computed using a dielectric matrix with 1798 bands on a $6 \times 6 \times 1$ k-point grid with 5 Ry screening cutoff. The absorption spectrum, electron-hole transitions, and exciton wavefunctions and energies were evaluated by interpolation of the interaction kernel onto a $18 \times 18 \times 1$ grid, with light polarization along the σ^+ direction. The absorption was

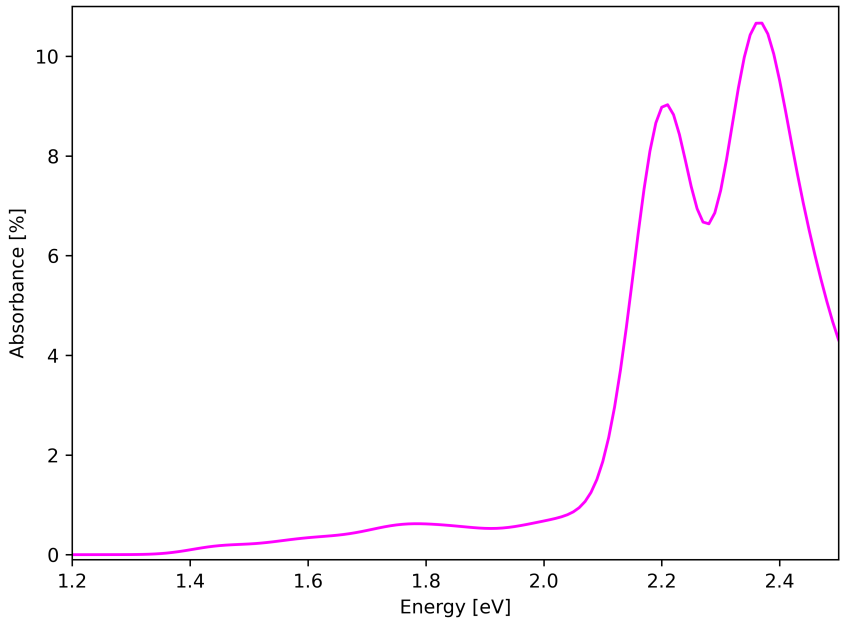

FIG. S1. Calculated absorbance spectrum of the $MoS_2 + V_S$ system under σ^+ polarized light.

calculated using [6]:

$$\epsilon_2(\omega) = \frac{16\pi^2 e^2}{\omega^2} \sum_S \left| f^S_{\sigma^+} \right|^2 \delta\left(\omega - \Omega^S\right), \tag{1}$$

where the delta function is broadened to a 50 meV FWHM Gaussian and the absorption oscillator strength is calculated by:

$$f^S_{\sigma^+} = \frac{1}{\sqrt{2}}(1, i, 0) \cdot \sum_{vc\mathbf{k}} A^S_{vc\mathbf{k}} \langle v\mathbf{k} | -i\nabla | c\mathbf{k} \rangle. \tag{2}$$

where $\frac{1}{\sqrt{2}}(1, i, 0)$ is the direction of the light polarization. The calculated absorbance at the σ^+ direction, as a function of energy, can be seen in Fig. S1.

II. Calculation of magnetic properties

Single-particle magnetic moments were calculated following Refs. [11, 12]. The orbital part of the magnetic moment was calculated using:

$$m^{orb}_{n\mathbf{k}} = -\frac{i\mu_B}{m_e} \sum_{n' \neq n} \left(\frac{\langle \psi_{n\mathbf{k}} | \hat{p}_x | \psi_{n'\mathbf{k}} \rangle \langle \psi_{n'\mathbf{k}} | \hat{p}_y | \psi_{n\mathbf{k}} \rangle}{E_{n'\mathbf{k}} - E_{n\mathbf{k}}} - \frac{\langle \psi_{n\mathbf{k}} | \hat{p}_y | \psi_{n'\mathbf{k}} \rangle \langle \psi_{n'\mathbf{k}} | \hat{p}_x | \psi_{n\mathbf{k}} \rangle}{E_{n'\mathbf{k}} - E_{n\mathbf{k}}} \right), \tag{3}$$

where μ_B is Bohr's magneton and m_e is the electron mass. $\psi_{n\mathbf{k}}$ is the wavefunction of band n at k-point k and $\hat{p}_i$ is the momentum operator in direction i. The momentum operator matrix

elements were calculated with DFT using Quantum Espresso [4]. $E_{n\mathbf{k}}$ is the energy of band n at k-point k, calculated within DFT and corrected to the GW results using a scissors-shift operator. Degeneracies at $E_{n\mathbf{k}} = E_{n'\mathbf{k}}$ were not included in the summation as they are vanishing in the examined bands, except for strictly at the $\bar{\Gamma}$ point. For this reason, the $\bar{\Gamma}$ point analysis includes a small shift, $k = (0, 0.056, 0)$. The orbital magnetic moments computed on a bandstructure k-path and shown as colors in the presented bandstructures were calculated by summation over 2300 spinor states. Within the GW-BSE calculations we used a summation over 2000 spinor states. GW corrections for the orbital magnetic moments were calculated using DFT energies in the denominator of Eq. 3 and then applying a GW-based scissors shift to correct the energy gaps at the $\bar{K}$ point to the computed GW gaps. Figure S2 shows the computed orbital magnetic moments within DFT and with the corrected GW-based scheme. Here, magenta dots show the orbital magnetic moments calculated with DFT energies in Eq. 3 and the orange dots correspond to the orbital magnetic moment calculated with the GW-based scissors-shifted energies. The valence band is shown by the dashed grey line. All exciton magnetic moments were computed with the GW-based method.

The spin magnetic moments were calculated using:

$$m_{n\mathbf{k}}^{spin} = -\frac{e g_e}{2m_e} \langle \psi_{n\mathbf{k}} | \sigma_z | \psi_{n\mathbf{k}} \rangle \,, \tag{4}$$

where e is an elementary charge and g_e is the free electron g-factor. All presented calculations of the magnetic properties were performed assuming a magnetic field perpendicular to the monolayer plane, in the $\hat{z}$ direction. σ^z is the Pauli matrix in the $\hat{z}$ direction and the expectation value was calculated using Quantum Espresso. The total (net) magnetic moment was then evaluated through the summation of the orbital and spin parts,

$$m_{n\mathbf{k}} = m_{n\mathbf{k}}^{orb} + m_{n\mathbf{k}}^{spin}. \tag{5}$$

The results of the different components of the magnetic moment are shown in Fig.S3. Figure S3a shows the convergence of the orbital magnetic moment with respect to the number of bands used in the summation in Eq.3 for 4 pristine-like bands and 4 in-gap defect bands (shown in different colors), at point . Figure S3b shows the orbital magnetic moment by color on a chosen k-path. Figure S3c shows the spin magnetic moment along the same k-path. Figure S3d shows the total magnetic moment, calculated by adding the orbital and the spin parts, on the same k-path.

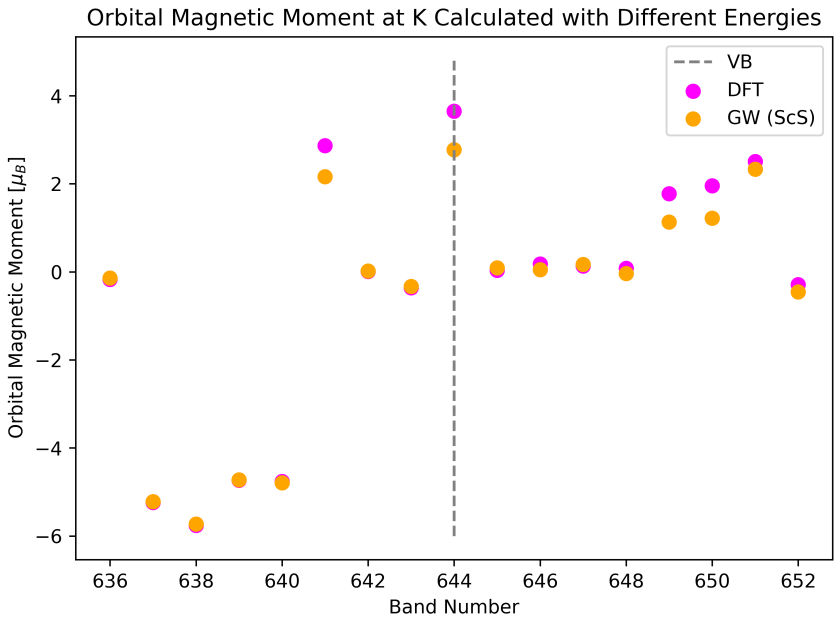

FIG. S2. Orbital magnetic moment of defect-MoS_2 at $\bar{K}$ of different bands using two different energies in Eq.3, DFT energies for all bands (magenta) or DFT energies for occupied bands and a scissors shift correction to the unoccupied bands (orange). The summation in Eq.3 was carried over 2300 bands. The valence band is shown by the dashed grey line.

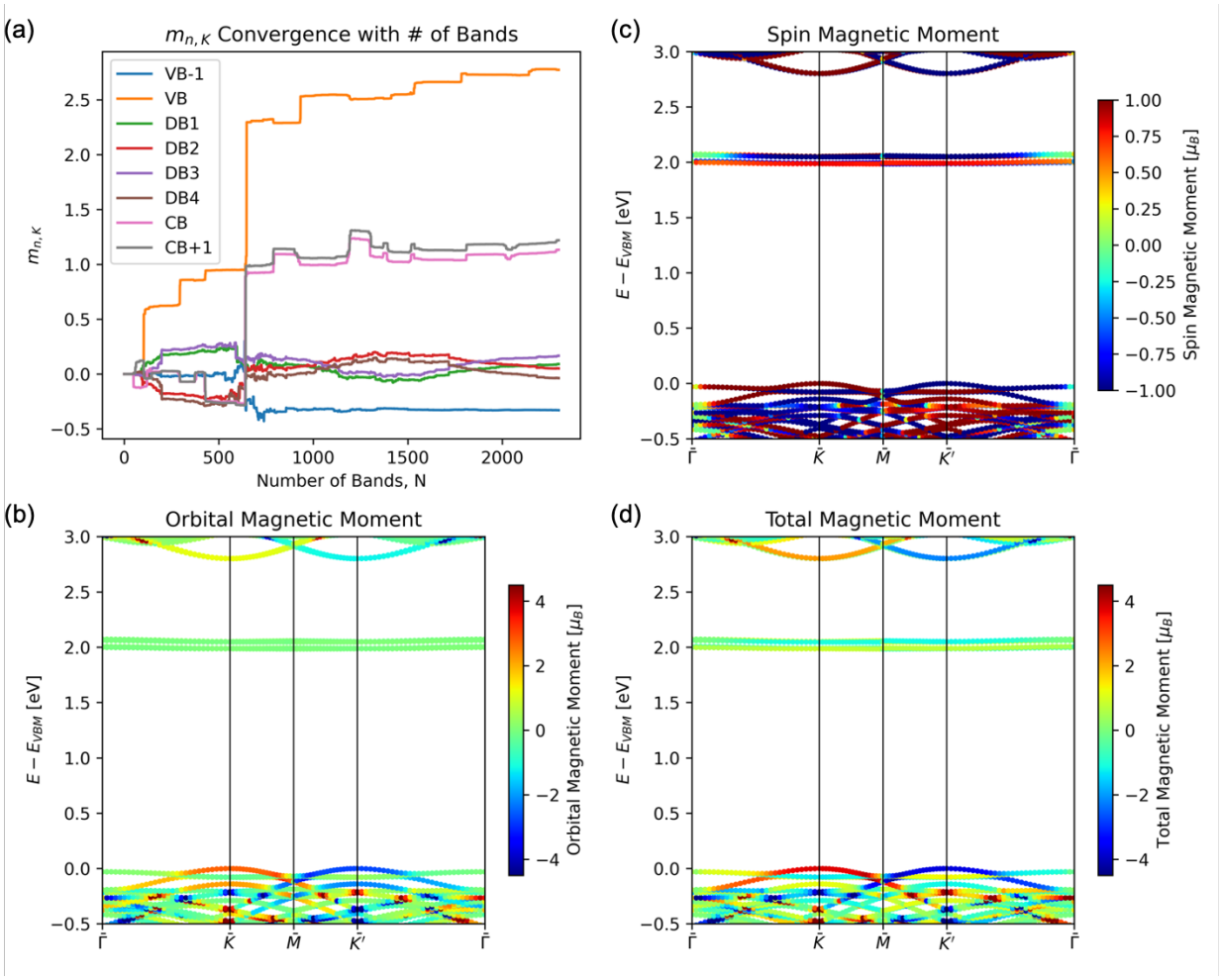

FIG. S3. (a): Convergence of the orbital magnetic moment at point for different bands, with the number of bands taken for the summation in Eq.3 for neutral-charge MoS_2 supercell with a sulphur vacancy. (b): Orbital magnetic colored on a band structure, calculated using Eq.3 with 2300 bands in the summation. (c): Spin magnetic moment colored on a band structure, calculated using Eq.4. (d): Total magnetic moment colored on a band structure, calculated using Eq.5. The calculation of the orbital magnetic moment in this figure is with DFT energies with a k-independent scissors shift correction using GW results for the unoccupied bands.

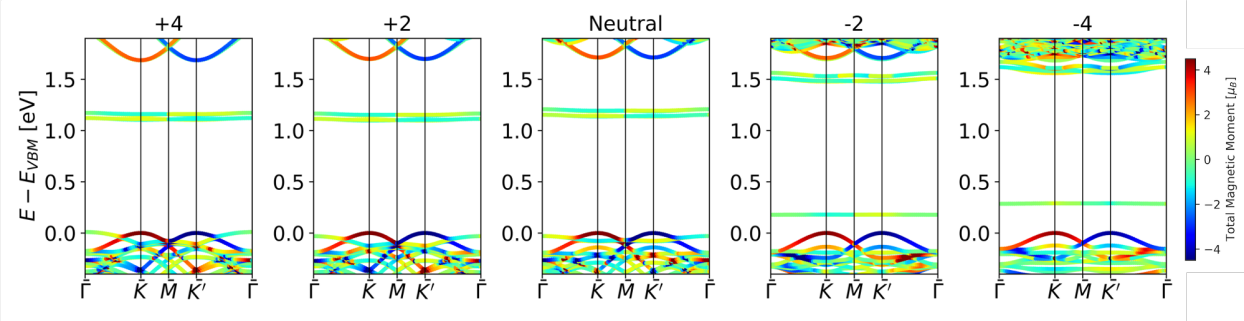

FIG. S4. Total magnetic moment in supercells with different total charges, colored on DFT bandstructures. The calculations here were done only within DFT, without scissors shift or other GW results.

III. Effect of defect charging

Figure S4 shows the DFT bandstructure of the examined MoS_2 with chalcogen vacancies, and upon electronic charging with a total charge of ± 2 and ± 4 per vacancy, in units of electron charge. Colors represent the total magnetic moment of each band at each k-point, similar to Fig S3. The charging mostly change the position of the defect bands relative to the pristine-like bands and affects the pristine band shape, most notably in the ± 4 systems. In the -2 charged system, the occupied defect bands are lifted in energy compared to the pristine-like valance band, throughout the Brillouin zone. This lifting removes the mixing of the occupied defect band with the pristine-like bands at the valence region. This is expected to reduce the exciton mixing of low-lying, defect-induced excitons; However, as we discuss in the main text, the $\bar{A}$ region mixing is expected to remain.

[1] W. Kohn and L. J. Sham, Phys. Rev. **140**, A1133 (1965).

[2] J. P. Perdew, K. Burke, and M. Ernzerhof, Phys. Rev. Lett. **77**, 3865 (1996).

[3] P. Giannozzi *et al.*, J. Phys. Condens. Matter **21**, 395502 (2009).

[4] P. Giannozzi *et al.*, J. Phys. Condens. Matter **29**, 465901 (2017).

[5] M. J. van Setten, M. Giantomassi, E. Bousquet, M. J. Verstraete, D. R. Hamann, X. Gonze, and G.-M. Rignanese, Comput. Phys. Commun. **226**, 39 (2018).

[6] J. Deslippe, G. Samsonidze, D. A. Strubbe, M. Jain, M. L. Cohen, and S. G. Louie, Comput. Phys. Commun. **183**, 1269 (2012), 1111.4429.

[7] M. S. Hybertsen and S. G. Louie, Phys. Rev. B **34**, 5390 (1986).

[8] F. H. da Jornada, D. Y. Qiu, and S. G. Louie, Phys. Rev. B **95**, 035109 (2017), 1610.06641.

[9] S. Refaely-Abramson, D. Y. Qiu, S. G. Louie, and J. B. Neaton, Phys. Rev. Lett. **121**, 167402 (2018).

[10] M. Rohlfing and S. G. Louie, Phys. Rev. B **62**, 4927 (2000); Phys. Rev. Lett. **81**, 2312 (1998).

[11] T. Woźniak, P. E. F. Junior, G. Seifert, A. Chaves, and J. Kunstmann, Phys. Rev. B **101**, 235408 (2020).

[12] T. Deilmann, P. Krüger, and M. Rohlfing, Phys. Rev. Lett. **124**, 226402 (2020).